L x rays emitted from multiply ionized holmium atoms

V. Horvat,* R. L. Watson, J. M. Blackadar, A. N. Perumal, and Yong Peng
Cyclotron Institute and Department of Chemistry, Texas A&M University, College Station, Texas 77843-3366, USA
(Received 4 November 2004; published 22 June 2005)

Spectra of *L* x rays emitted from Ho targets bombarded by 10 keV electrons and 6 MeV/amu C, Ne, Ar, Kr, and Xe ions were measured in high resolution using a curved crystal spectrometer. The spectra were analyzed in order to examine the systematic evolution of the *L* x-ray satellite structure as a function of projectile atomic number. Scaling rules are established for the apparent average *M*-shell spectator vacancy fraction and apparent average double to single *L*-vacancy population ratio at the time of *L* x-ray emission. The results are compared to those obtained for *K*-shell ionizing collisions and with predictions of the geometrical model.

DOI: 10.1103/PhysRevA.71.062709 PACS number(s): 34.50.Fa, 32.30.Rj

I. INTRODUCTION

Early comprehensive studies of satellite structure appearing in *L* x-ray spectra were carried out by Richtmyer [1] and co-workers, Parratt [2,3], and Randall and Parratt [4] over 65 years ago using x-ray fluorescence and electron bombardment. As many as ten semiresolved satellite peaks were observed on the high-energy side of the $L\alpha_1$ lines of Mo through Ba, and similar structures were found above the $L\beta$ and $L\gamma$ lines of Ag. Shortly after the discovery of *L* x-ray satellites, Coster and Kronig [5] suggested that these lines originate from double vacancy states created by $L_1 \rightarrow L_2\, M_{45}$ and $L_1 \rightarrow L_3\, M_{4,5}$ nonradiative transitions. Subsequent work by Richtmyer and Ramberg [6] confirmed the plausibility of this hypothesis and presented theoretical predictions of the complex multiplet structure associated with the *LM* double-vacancy satellites of $L\alpha_1$ and $L\beta_2$ in Au. Other mechanisms contributing to the production of *L* x-ray satellites were later recognized to be the shake-up and shake-off processes [7]. Double collisions were found to contribute as well. Over the intervening years, interest in this subject has endured and notable progress in understanding the structure and properties of *LM* double-vacancy satellites is described in Refs. [8–11].

The present paper concerns *L* x-ray satellite structure arising from multiple vacancy production by heavy ion impact. Following the published high-resolution measurements of ion-excited *L* x-ray spectra by Der *et al.* [12], Olsen *et al.* [13] obtained spectra that revealed intense satellite structure indicative of the presence of multiple *M* vacancies. In their spectrum of Sn *L* x rays excited by 30 MeV oxygen ion impact, the satellite average energies disclosed the presence of four to five spectator *M* vacancies. The intensity of the satellite peaks was substantially greater than that of the (single-vacancy) diagram lines.

Because of the complexity of multiple-vacancy *L* x-ray satellite structure, however, only a few subsequent studies have focused on this topic. The effects of chemical environment on the relative intensity profiles of ion-induced *L* x-ray satellites have been examined by Rosseel *et al.* [14,15]. The gross features and average energies of Ta, Au, and Th *L* x-ray satellites produced in 4 MeV/amu Kr ion collisions have been discussed by Heitz *et al.* [16]. Recently, Czarnota *et al.* [17] have used a high-resolution von Hamos spectrometer to study the $L\alpha$ and $L\beta$ multiple-vacancy satellite structure of Mo and Pd atoms excited by O and Ne ions. These authors compared their spectra to the predictions of multiconfigurational Dirac-Fock calculations that took into account the complex multiplet structure arising from one- and two-spectator *M* vacancies. The calculations were in reasonable agreement with the Pd satellite structure observed in collisions by 376 MeV O ions, which was dominated by single *M*-vacancy configurations. The satellite structure observed by these authors in collisions by 178 MeV Ne ions was found to contain large contributions from configurations involving up to four *M* vacancies. Because of the unmanageable complexity of the multiplet structure for configurations involving more than two spectator *M* vacancies, this spectrum had to be analyzed using calculated average-of-configurations satellite energies and the assumption that the distribution of spectator *M* vacancies is binomial. Recently, the systematics of the *M*- and *N*-shell ionization probabilities as a function of projectile and target atomic number and projectile energy have been deduced from low-resolution measurements employing a semiconductor detector [18]. An elaborate method of analysis was developed to extract ionization probabilities from the energy shifts of the unresolved x-ray peaks containing the $L\gamma$ diagram lines and satellites.

In the present work, *L* x-ray spectra of Ho were measured using a curved crystal spectrometer, employing second-order diffraction from a LiF crystal. The spectra were excited by 10 keV electrons and 6 MeV/amu C, Ne, Ar, Kr, and Xe ions. The main objective of these measurements was to study the systematic evolution of the *L* x-ray satellite structure with increasing projectile atomic number. Based on a relatively simple interpretation of the structure in the measured spectra, an analysis procedure was developed that reproduced the shape of the spectra with reasonably good accuracy. This procedure was also used to determine the apparent average *M*-shell and outer-shell spectator vacancy fractions at the time of *L* x-ray emission. The results are compared to the predictions of the geometrical model and with apparent average spectator *L*-vacancy fractions at the time of *K* x-ray

*Electronic address: V-Horvat@tamu.edu

emission for atoms having L binding energies comparable to the M binding energies of Ho. Relative contributions to the x-ray yields from ions having more than one initial-state vacancy in the L shell were examined as well.

II. EXPERIMENT

Beams of 6 MeV/amu C^{2+}, Ne^{3+}, Ar^{6+}, Kr^{12+}, and Xe^{18+} ions were extracted from the Texas A&M K-500 superconducting cyclotron, charge analyzed, collimated, and focused to a ~3 mm diam spot onto the target oriented at 45° with respect to the beam direction. The focusing was accomplished with the aid of a zinc-cadmium sulfide phosphor and a closed-circuit television system. During the data acquisition, the beam intensity was monitored by measuring the current from the target or from a Faraday cup placed directly behind the target.

The measurements were performed with a thick metallic Ho foil (~100 mg/cm^2). However, because of x-ray absorption and projectile energy dependence of the L x-ray production, the estimated effective mean target depth for Ho L x-ray detection ranges from 2.7 mg/cm^2 for the C-induced spectrum to 6.0 mg/cm^2 for the Xe-induced spectrum. The effective mean projectile energy was estimated at 5.5 MeV/amu in all the cases studied here. The effects of projectile energy loss on the spectral features of interest were found to be negligible. The details will be explained in Sec. V.

A 12.7 cm Johansson-type curved crystal spectrometer with the focal circle oriented perpendicular to the beam axis was used to measure the x-ray spectra. The x rays diffracted in second order from a LiF(200) crystal were counted by a flow-proportional counter operating with P-10 gas [argon (90%) and methane (10%) at 1 atm]. Control of the spectrometer-stepping motor was accomplished by means of a custom-designed electronic module and a personal computer equipped with a dedicated multiscaler expansion card and the accompanying software. Before each run series, the crystal angle and focal circle were manually adjusted to maximize the intensity of Ho L x rays.

An energy calibration was performed during each run series after completing the crystal angle and focal circle adjustments. The $K\alpha_1$, $K\alpha_2$, and $K\beta_1$ diagram lines of Co, Ni, and Cu were used for these calibrations in addition to the $L\alpha_1$, $L\beta_1$, and $L\beta_2$ diagram lines of Ho. It was found previously that diagram lines (due to transitions between single-vacancy states), can be quite prominent when the target is bombarded by heavy ions [19,20]. The single-vacancy states are produced primarily by high-energy electrons ejected in the primary collisions or by high-energy photons subsequently emitted from the projectile or target. In general, overlapping contributions from multiple-vacancy states excited in ion-atom collisions, were small and did not shift the calibration peaks by more than 1 eV. The spectrometer energy resolution (FWHM) for the Ho $L\alpha_1$ line excited by 10 keV electron bombardment was determined to be 9.3 eV (based on the Gaussian width of a Voigt function used to fit the corresponding peak).

III. INTERPRETATION OF THE SPECTRA

The gross features of the Ho L x-ray spectra are compared in Fig. 1. Vertical dashed lines indicate the positions of the nine most prominent L x-ray diagram lines of Ho in the energy range between 6400 and 8400 eV. Their spectroscopic identifications and corresponding initial- and final-state vacancy configurations are listed in Table I. The solid line at the far right in Fig. 1 shows the position of the L_3 absorption edge at 8068 eV.

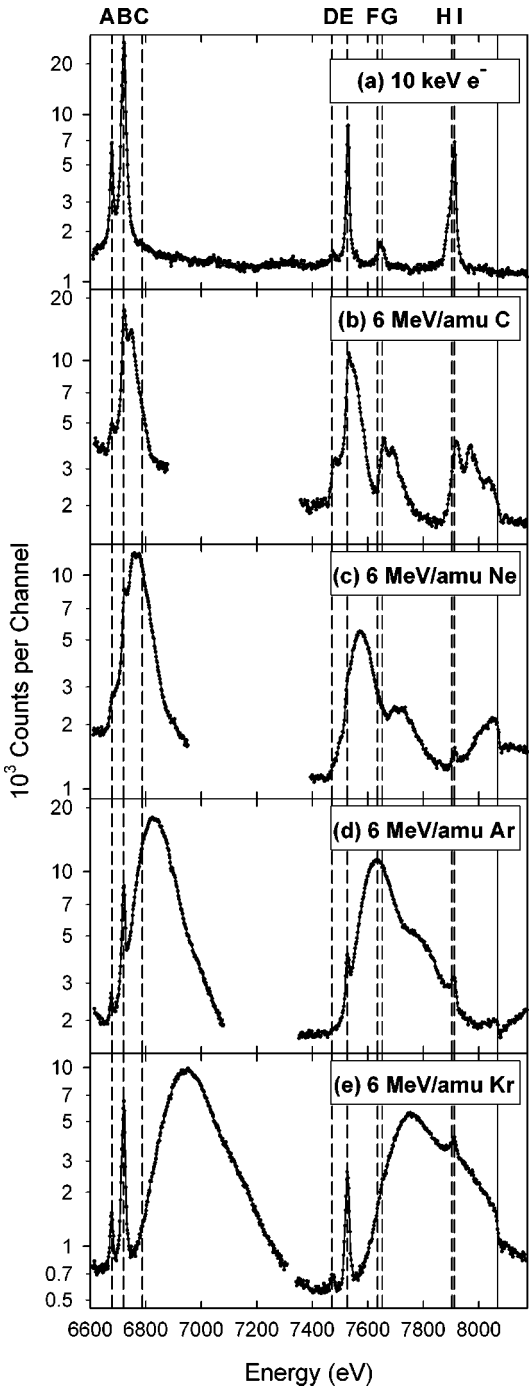

FIG. 1. Spectra of L x rays emitted from a Ho target under bombardment by (a) 10 keV electrons and 6 MeV/amu beams of (b) C, (c) Ne, (d) Ar, and (e) Kr. The vertical dashed lines indicate the energy positions of the nine most prominent L x-ray diagram lines (see Table I). The L_3 absorption edge is shown by the vertical solid line.

TABLE I. The most prominent *L* x-ray diagram lines of Ho in the energy range between 6400 and 8400 eV.

Line	Transition	Energy (eV)[a]	Natural width (eV)[b]	Relative intensity[c]	Label in Fig. 1
$L\alpha_1$	$L_3 \rightarrow M_5$	6719.7	5.1	100.0	B
$L\alpha_2$	$L_3 \rightarrow M_4$	6678.5	5.1	11.1	A
$L\beta_6$	$L_3 \rightarrow N_1$	7635.8	9.6	1.1	F
$L\beta_2$	$L_3 \rightarrow N_5$	7911.4	6.8	18.2	I
$L\beta_{15}$	$L_3 \rightarrow N_4$	7902.9	7.2	2.0	H
$L\beta_1$	$L_2 \rightarrow M_4$	7525.7	5.2	100.0	E
$L\eta$	$L_2 \rightarrow M_1$	6786.9	17.5	2.2	C
$L\beta_3$	$L_1 \rightarrow M_3$	7651.8	12.3	100.0	G
$L\beta_4$	$L_1 \rightarrow M_2$	7471.1	10.8	62.6	D

[a]Ref. [21].
[b]Derived from the data in Ref. [22].
[c]Estimated using data from Ref. [23].

The spectrum obtained by electron bombardment [Fig. 1(a)] shows (for the most part) the peaks due to Ho *L* x rays emitted by singly ionized atoms (diagram lines). They were found to be accurately represented by Voigt functions and their centroids agreed (within ±2 eV on average) with the corresponding recommended transition energies of Deslattes *et al.* [21]. The widths of the observed peaks were found to be in agreement (within ±2 eV on average) with the corresponding natural line widths derived from the recommended level width values of Campbell and Papp [22]. Also, the relative intensities of the peaks resulting from transitions to the same *L* subshell were found to be within a few percent of the relative transition rate values recommended by Salem *et al.* [23]. The latter observation indicates that the product of the spectrometer-detection efficiency and the x-ray transmission probability from the target did not vary significantly over the energy range of interest. The data referenced above are also listed in Table I.

Target atom *L*-shell ionization by heavy ions is usually accompanied by electron removal from higher shells. Consequently, the resulting x-ray peaks (which are commonly referred to as satellite peaks) are broadened and shifted relative to those corresponding to diagram transitions. Furthermore, the peak shapes can be very complex due to (i) variations in the initial state vacancy configuration at the time of x-ray emission and (ii) the complicated multiplet structure that arises from the coupling of initial and final state angular momenta. In Ho, the satellite transition energies are shifted, on average, by only a few eV per vacancy in shells higher than the *M*-shell (collectively referred to here as outer shells). For $L \rightarrow M$ transitions, these shifts are smaller than the natural widths of the transitions involved, and for $L \rightarrow N$ transitions they are only slightly larger. Consequently, peaks due to transitions between states involving multiple outer shell vacancies cannot be resolved from each other or from the corresponding diagram lines. Therefore, the structure observed in the vicinity of the diagram transition energy includes contributions both from the diagram transitions in atoms ionized by secondary radiation and from the satellite transitions in atoms that acquire single *L*-shell and multiple outer-shell vacancies in heavy-ion-atom collisions.

If, on the other hand, heavy-ion-induced Ho *L*-shell ionization is also accompanied by single or multiple *M*-shell ionization, the resulting satellite peaks are additionally shifted up in energy by 20 to 50 eV per *M* vacancy, depending on the transition type. They may or may not be resolved, depending on how their shifts compare to their widths. For a given number of spectator *M* vacancies, the corresponding satellite peak width depends, for the most part, on the average number of outer-shell vacancies and the extent of multiplet splitting. In the spectrum excited by carbon ions [Fig. 1(b)], the peaks on the high-energy sides of the $L\alpha_1$, $L\beta_3$, and $L\beta_2$ lines mainly contain satellite transitions from initial states having a single *L* vacancy plus a single *M* vacancy.

The complex multiplet structure, resulting from the angular momentum coupling of multiple *L* plus *M* vacancy states, together with the additional modifications imposed by vacancies in the outer shells, makes a detailed analysis of the satellite structure an impossible task [17]. Nevertheless, the spectrum of *L* x rays induced by C ions [Fig. 1(b)] does exhibit definite structural features that (as will be shown below) strongly correlate with the transition energies expected for L^1M^0, L^1M^1, and L^1M^2 initial state vacancy configurations with additional outer-shell vacancies. In this paper, the satellite peaks will be labeled using the notation $L^i\xi M^j$, where L^iM^j denotes the initial state vacancy configuration of the *L* and *M* shells, while ξ identifies the transition (e.g., $\xi = \alpha_1, \beta_{2,15}, \eta, \ldots$). Note that *j* is also the number of *spectator* *M* vacancies for each transition.

Apparently, the *L* x rays that predominantly contribute to the spectrum in Fig. 1(b) are emitted in the presence of a small number of outer-shell vacancies. This is evidenced by relatively small energy shifts of the $L^1\xi M^0$ satellites from the corresponding diagram transition energies and a relatively small increase in their widths compared to the corresponding diagram-transition peaks. The energy shift of the $L^1\beta_{2,15}M^0$ satellite is somewhat larger than the others because the transition in this case involves an *N* electron whose binding energy is less sensitive to the presence of spectator vacancies. According to calculations performed with the multiconfigu-

rational Dirac-Fock (MCDF) code of Desclaux [24], a single N spectator vacancy causes the $L\alpha_1(L_3 \rightarrow M_5)$ and $L\beta_2(L_3 \rightarrow N_5)$ transitions to shift up in energy, on average, by 2.3 and 9.2 eV, respectively.

L x-ray satellite peaks are the dominant features appearing in the spectra obtained with Ne, Ar, and Kr ions [shown in Figs. 1(c)–1(e), respectively]. The same is true for the spectrum obtained with Xe ions (not shown). It is evident that the degree of multiple ionization in the M shell of the target atom increases rapidly with the projectile atomic number. Consequently, the centroids of the satellite peak distributions (including all satellites, regardless of the corresponding number of spectator M vacancies) are shifted higher in energy and the widths of the satellite peak distributions increase. In addition, because of the increased degree of multiple ionization in the outer shells and the increasingly complex multiplet structure, satellite peaks corresponding to a given number of spectator M vacancies are no longer resolvable. Apparently, the increase in the energy shifts of the satellite distribution centroids is larger than the corresponding increase in the distribution widths, so that the satellite distributions contribute less in the vicinity of the corresponding diagram transition energies. On the other hand, the contributions from secondary ionization are substantial, and so the peaks due to diagram transitions become prominent. This is clearly the case for the $L\alpha_2$, $L\alpha_1$, $L\beta_1$, and $L\beta_2$ diagram lines in the Ar- and Kr-induced spectra [Figs. 1(d) and 1(e), respectively]. The same is true for the Xe-induced spectrum (not shown), which displays somewhat larger satellite energy shifts (as expected from the trend), but otherwise is not essentially different from the Kr-induced spectrum.

IV. ANALYSIS OF THE SPECTRA

Interpretation of the diagram line contributions in the spectra excited by heavy ions was facilitated by a least-squares analysis of the Ho L x-ray spectrum obtained by 10 keV electron bombardment [Fig. 1(a)]. In this analysis, each peak was represented by a Voigt function with variable Lorentzian width. To simplify the fitting procedure, the Gaussian widths of the Voigt functions, representing (for the most part) the resolution of the spectrometer, were assumed to be the same for all the diagram lines. The peak profiles determined in this way were subsequently used in the analysis of the diagram lines in the spectra of Ho L x rays induced by heavy ions.

The analysis procedure for the satellite peaks was developed using the spectrum of Ho L x rays induced by 6 MeV/amu C ions [shown in Fig. 1(b)] because the satellite peak structure in this spectrum contains the most resolved structural features. The same analysis procedure was then applied to the other spectra. To ensure stability of the least-squares fitting process and reproducibility of the results, the number of adjustable parameters was kept at a minimum. For example, the peak centroids of all the satellite peaks in a given spectrum were varied using only one free parameter, while their relative intensities were fitted using only four independent parameters. Gaussian widths of all $L\alpha_2$, $L\alpha_1$, and $L\eta$ satellite peaks combined were determined with only two parameters. Peaks due to the presence of a spectator vacancy in the L shell at the time of L x-ray emission were taken into account using only one additional fitting parameter. A detailed description of the method is given in the Appendix.

As mentioned in the Appendix, the relative number of counts in each $L^1\xi M^j$ satellite peak for a given transition (specified by ξ) was assumed to follow a binomial distribution as a function of the number of spectator M vacancies (j). This assumption was justified by the fact that, in practice, it yielded good representations of the measured spectra of x rays emitted from multiply ionized atoms. In order to convert the measured x-ray yields to initial *vacancy* yields, corrections must be applied to account for vacancy rearrangement between the time of collision and the time of L x-ray emission. Also, it is necessary to take into account the fact that fluorescence yields depend on the spectator vacancy configurations at the time of L x-ray emission. Although approximate methods for accomplishing these tasks have been developed and applied in the analysis of K x-ray spectra [19,25], the much more complex decay scheme for L-vacancy decay, together with large uncertainties associated with available theoretical transition rates and their scaling, makes such an analysis for L x-ray spectra impractical at the present time. Therefore, the centroid of the binary distribution determined in the present work (p_M^x) represents the apparent average M-shell spectator vacancy fraction at the time of L x-ray emission. Under the assumption that the net effect of vacancy rearrangement and fluorescence yields does not depend significantly on the number of contributing M-shell spectator vacancies (since the two effects tend to counteract each other), p_M^x is approximately equal to the M-shell ionization probability per electron (p_M) in L-shell ionizing collisions, as defined in the framework of the independent electron approximation [26].

The quality of the fit achieved in the case of the Ho L x-ray spectrum excited by 6 MeV/amu C ions [Fig. 1(b)] is demonstrated in Figs. 2(a) and 2(b), where the experimental data points, fitted curve, background component curve, and five $L^1\xi M^j$ satellite peaks (with $j=0$–4) are shown. Satellite peaks for $j>4$ and $L^2\xi M^j$ satellites are too small to be seen. The diagram lines are not shown because their contribution was found to be negligible in this spectrum. This is not surprising because (i) the secondary electron yield produced by C ions is expected to be much smaller than the yields produced by the heavier projectiles and (ii) the degree of Ho ionization produced by carbon ions is relatively low, so that only a very small fraction of the satellite ($L\beta_{2,15}$) x-ray spectrum extends above the L_3 absorption edge. Although the entire spectrum was fit simultaneously, the two spectral regions are shown separately [Figs. 2(a) and 2(b)] in order to reduce the amount of empty space and enhance the details.

In a similar way, Figs. 2(c) and 2(d) show the fit of the Ho L x-ray spectrum excited by 6 MeV/amu Ne ions. In this spectrum, the individual contribution from six $L^1\xi M^j$ satellites can be clearly seen. The same holds for the diagram lines (mainly $L\alpha_2$, $L\alpha_1$, $L\beta_1$, and $L\beta_2$) and the combined contribution from the $L^2\xi M^j$ satellites.

Components of the spectrum of Ho L x rays induced by 6 MeV/amu Kr ions are shown in Figs. 3(a) and 3(b) to

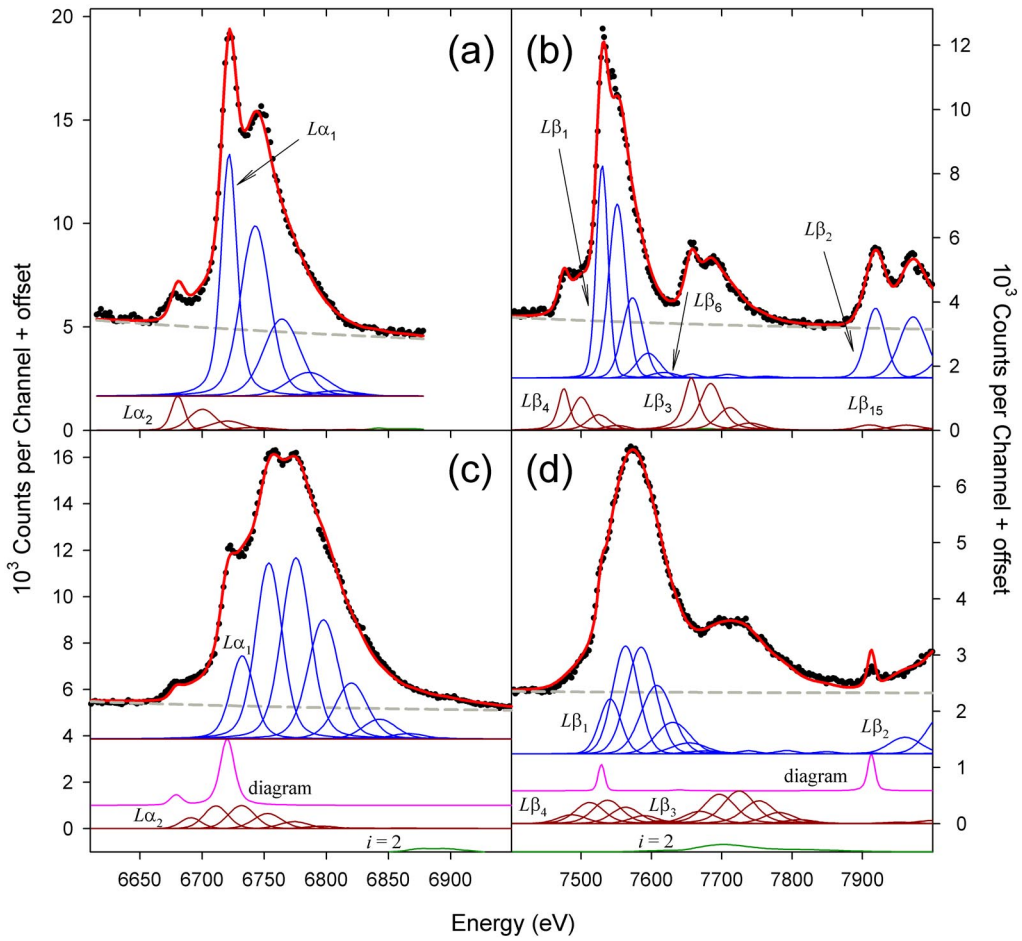

FIG. 2. (Color online) Fit of the Ho *L* x-ray spectrum excited by (a) and (b) 6 MeV/amu C ions and (c) and (d) 6 MeV/amu Ne ions showing the experimental data points (black), overall fitted curve (red), background component curve (gray), and individual $L^1\xi M^j$ satellite peaks (blue and brown). Some of the peaks are offset in the vertical direction to avoid excessive overlapping. Only one representative peak in each group is labeled in order to avoid overcrowding. The remaining curves, as labeled, represent the combined contribution from the *L* x-ray diagram lines (magenta) and the combined contribution from the $L^2\xi M^j$ satellite peaks (green).

illustrate the features that are not as prominent in the spectra shown in Fig. 2. Here the diagram peaks contribute substantially and some of them ($L\alpha_2$, $L\alpha_1$, and $L\beta_1$) are well separated from the corresponding $L^1\xi M^j$ satellite groups, which peak at much higher energies. In addition, the $L^1\xi M^j$ satellite distributions do not display any structural features because the widths of the individual $L^1\xi M^j$ satellite peaks (not shown) are large compared to their separations. The $L^1\beta_3 M^j$ satellite distribution appears as a shoulder on the high-energy side of the $L^1\beta_1 M^j$ satellite distribution. Although the $L^2\xi M^j$ satellite distributions cannot be resolved from the $L^1\xi M^j$ satellite distributions, their contributions are more substantial in this spectrum than in the spectra shown in Fig. 2. Contributions from the $L^3\xi M^j$ satellite distributions are relatively small and also unresolved, but they can be clearly identified.

In addition to providing energy calibrations for the analyses of the Ho *L* x-ray spectra, the spectra of *K* x rays measured for Co, Ni, and Cu targets allowed a comparison to be made of the apparent average *L*-shell spectator vacancy fraction (p_L^x) for *K*-vacancy-producing collisions with p_M^x for *L*-vacancy-producing collisions in atoms having comparable transition energies. The *K* x-ray spectra were analyzed by applying the same procedures used in the analyses of the *L* x-ray spectra. An example of a fit to a spectrum of Co *K* x rays excited by Kr ions, showing the contributions from the $K\alpha_1$ and $K\alpha_2$ diagram lines, $K^1\alpha_1 L^i$ satellites, and $K^1\alpha_2 L^i$ satellites, is given in Fig. 4.

V. RESULTS AND DISCUSSION

A summary of the results of primary interest is presented in Table II. Listed in the first three rows are the p_L^x values obtained in the analyses of the Co, Ni, and Cu *K* x-ray spectra. The next two rows contain the values of p_M^x and p_{N+}^x obtained in the analyses of the Ho *L* x-ray spectra. The p_{N+}^x values were calculated by dividing the average number of spectator outer-shell vacancies (κ) determined in the fits by the maximum value of 39, and hence they represent the apparent average vacancy fractions for the *N* shell plus all shells above it.

The sixth and seventh rows of Table II list the quantities $R^K{}_{2/1}$ and $R^L{}_{2/1}$. The former is the apparent average double-to-single *K*-vacancy population ratio at the time of *K* x-ray emission in Co, Ni, and Cu, whereas the latter is the apparent

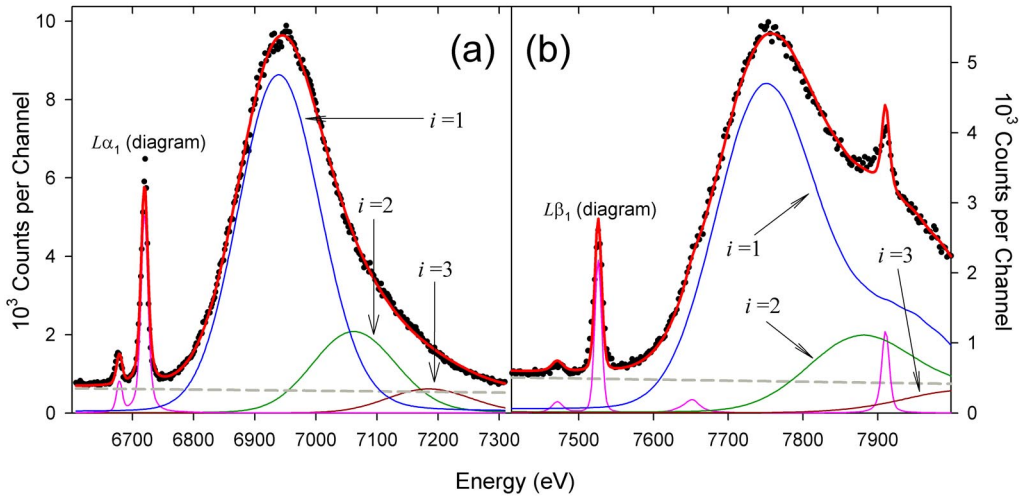

FIG. 3. (Color online) Fit of the Ho L x-ray spectrum excited by 6 MeV/amu Kr ions. The circles represent the measured data points; the solid lines represent the overall fit (red), the (combined) $L^i\xi M^j$ satellite groups [blue, green, and brown, shown separately for different numbers of initial L vacancies (i), as indicated] and (combined) contribution from the L x-ray diagram lines (magenta). Satellite peaks corresponding to different values of j are not shown individually, although they were included in the analysis as such. The dashed line (gray) represents the background.

average double-to-single L-vacancy population ratio at the time of L x-ray emission in Ho. Since a configuration with two K or L vacancies decays by the emission of a double- (K or L) vacancy satellite x ray followed by the emission of a single- (K or L) vacancy satellite x ray, these ratios were calculated by first subtracting the intensity of the double-vacancy satellites from the intensity of the single-vacancy satellites and then dividing the double-vacancy satellite intensity by this corrected single-vacancy satellite intensity. Under the assumption that the effects of vacancy rearrangement and fluorescence yields on the double- and single-vacancy decays are nearly the same and counteracting, this ratio is approximately equal to the ratio of the double- and single-vacancy production cross sections. For the cases in which triple L-vacancy satellite x rays contribute, the double-vacancy satellite intensity was corrected following the same logic. However, the single-vacancy satellite intensity for these cases was corrected by subtracting the intensity of the "uncorrected" double-vacancy satellites.

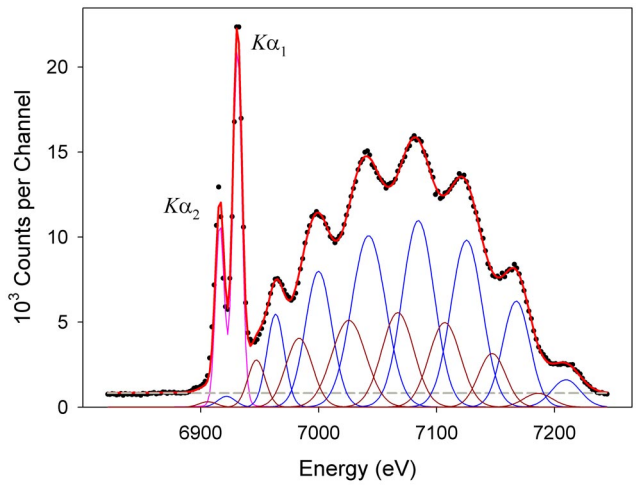

FIG. 4. (Color online) Spectrum of K x rays emitted from a thick Co target bombarded by 6 MeV/amu Kr ions. The circles represent the measured data points; the solid lines represent the overall fit (red), the contributions from $K\alpha_1$ and $K\alpha_2$ satellites (blue and brown, respectively), and the combined contribution from the $K\alpha_1$ and $K\alpha_2$ diagram lines (magenta). The dashed line (gray) represents the background.

The eighth and ninth rows in Table II show, respectively, the fraction of combined diagram x-ray intensity and the fraction of combined intensity of $L^i\xi M^j$ satellites for $i>1$ relative to the total L x-ray intensity. In cases where one or both of these fractions are substantial, estimation of p_M^x or p_M values from low-resolution spectra can lead to large errors.

According to the geometrical model [27], ionization probabilities per electron (p_n) for near-central collisions should lie on a universal curve when plotted as a function of the universal variable (X_n), given by

$$p_n = X_n^2/\{4.2524 + X_n^2[1 + 0.5\ \exp(-X_n^2/16)]\}, \qquad (1)$$

where

$$X_n = 4V[G(V)]^{1/2}Z_1/(nv_1). \qquad (2)$$

In Eq. (2), Z_1 is the projectile atomic number, v_1 is its speed in atomic units, n is the principal quantum number of the ionized target electron, $V=v_1/v_2$ is the scaled projectile speed (v_2 is the average target electron speed prior to ionization), and $G(V)$ is the binary encounter approximation (BEA) scaling function [28], originally formulated to describe the universal scaling of the cross sections for inner-shell ionization. The results of geometrical model calculations may vary based on the choice of the value adopted for Z_1 (e.g., the projectile nuclear charge or a screened effective charge), the electronic configuration of the target atom for calculation of v_2, and which one of the many available forms of the func-

TABLE II. Summary of results. Numbers in parenthesis denote the statistical error in the last digit of the result.

Parameter\Z_1	6	10	18	36	54
p_L^x (Co)	0.105(3)	0.232(3)	0.370(5)	0.49(2)	0.54(2)
p_L^x (Ni)	0.092(3)	0.205(3)	0.353(5)	0.50(2)	0.53(2)
p_L^x (Cu)	0.084(3)	0.216(3)	0.341(5)	0.47(2)	0.53(2)
p_M^x (Ho)	0.061(2)	0.116(1)	0.235(2)	0.419(4)	0.501(5)
p_{N+}^x (Ho)	0.070(2)	0.132(1)	0.265(2)	0.461(4)	0.546(5)
$R^K_{2/1}$			0.053(5)	0.086(8)	0.043(4)
$R^L_{2/1}$	0.00653(7)	0.0335(2)	0.123(2)	0.228(6)	0.215(2)
$I(L_x^{\text{diagr.}})/I(L_x^{\text{tot}})$	0.00201(4)	0.0434(2)	0.030(3)	0.0474(8)	0.0421(4)
$I(L_x^{i>1})/I(L_x^{\text{tot}})$	0.00643(7)	0.0300(1)	0.108(8)	0.208(3)	0.2141(7)

tion $G(V)$ is used. In the more fundamental approach, which was originally used to derive Eq. (1), the results also depend on the choice of electronic wave functions used and the chosen form of the ionization efficiency function (see Ref. [27] for details). In the present application, Z_1 is taken to be the projectile nuclear charge and v_2 is computed from the neutral atom binding energy [29]. (For L electrons, v_2 was calculated from the weighted average of L subshell binding energies.) The form of the function $G(V)$ employed here is one developed by Gryzinski, as presented in analytical form in Ref. [28].

The apparent average vacancy fractions (p_L^x, p_M^x, and p_{N+}^x) obtained in the present work are plotted in Fig. 5 as a function of the universal variable (X_n). The dashed solid line shows the predictions of the geometrical model [Eq. (1)]. Evidently, the scaling predicted by the geometrical model is appropriate, since the measured apparent average vacancy fractions do seem to follow a universal curve as a function of X_n. However, this universal curve is not in agreement with Eq. (1), which increasingly overestimates the experimental data points as X_n increases. The solid line in Fig. 5 is a logistic curve that has been fit to the data points and represents an empirical universal function for the apparent average vacancy fractions. It is given by

$$p_s^x = a/[1 + (b/X_n)^c], \tag{3}$$

where $a=0.579\pm0.016$, $b=1.86\pm0.11$, and $c=1.95\pm0.09$. Notably, at large values of X_n, the p_M^x values seem to systematically exceed those of p_L^x, which may indicate that the universality of the geometrical scaling breaks down at large X_n. Furthermore, the p_{N+}^x values deviate from the best-fit line more than the p_M^x values do. This is a consequence of the fact that, for large X_n, only p_M^x was varied independently in the spectral analysis fitting procedure, while p_{N+}^x was estimated from p_M^x (as explained in the Appendix) based on the dashed curve in Fig. 5, which has a larger slope as a function of X_n compared to the best-fit curve.

It is important to recognize that the geometric model predicts *ionization* probabilities per electron, whereas the present experiments measure apparent average vacancy fractions at the time of L x-ray emission. This fact may account for some of the deviations from a universal scaling described above. However, it cannot explain the large difference between the predicted geometrical model universal curve and the empirical universal curve in Fig. 5. It is estimated that the net result of vacancy rearrangement and fluorescence yield enhancement would be to increase the p_M^x and p_{N+}^x values by only about 10 to 20%, based on a previous analysis of these effects on the p_L^x values of a Cu target excited by 10 MeV/amu projectiles ranging from Ne to Bi [19].

It should be noted also that the measured values of p_L^x, p_M^x, and p_{N+}^x correspond to the effective average value of the projectile speed v_1, which was calculated by taking into account the projectile penetration depth dependence on (i) the

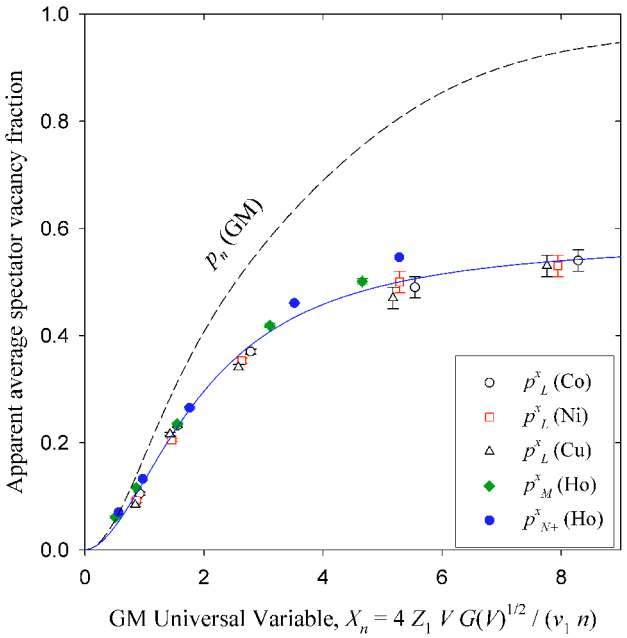

FIG. 5. (Color online) Ionization probabilities per electron (dashed curve) plotted as a function of the universal variable (X_n) according to the geometrical model [27]. The data points are experimental apparent average vacancy fractions obtained in analyses of Co, Ni, and Cu K x-ray spectra (p_L^x) and Ho L x-ray spectra (p_M^x and p_{N+}^x). Index $N+$ refers to Ho outer shells (N shell plus the shells above it). X_n was determined using Eq. (2) and expressed in atomic units.

projectile energy, (ii) the x-ray production cross section, and (iii) the x-ray transmission probability. Ziegler's method was used to estimate the projectile energy loss [30], whereas the x-ray production cross sections were approximated by the combined cross sections for direct ionization and ionization by nonradiative electron capture, calculated according to the perturbed stationary-state theory with corrections for energy loss, Coulomb deflection, and relativistic effects (ECPSSR theory) [31]. The current recommended values [32] were used for the x-ray attenuation coefficients. The effective average values of v_1 were subsequently used to determine the most appropriate values of X_n for the data points shown in Fig. 5. The calculations were performed for L_3 ionization and $L\alpha_1$ x rays (for $n=3$) and also for K ionization and $K\alpha_1$ x rays (for $n=2$). The uncorrected values of X_n were found to be as much as 5% lower than the corrected values.

In order to examine the effect of projectile energy loss and provide justification for employing a thick Ho target, the dependence of p_M^x on v_1 contained in the empirical universal curve [Eq. (3)] was used to calculate the effective average values of p_M^x by applying the same procedure described above for determining the effective average value of v_1. It was found that the largest difference between the effective average value of p_M^x and its "actual" value at the effective average projectile energy (for the cases studied here) was 0.0002 units, which is well below the statistical uncertainties listed in Table II.

In the determination of X_n, the average target electron speed prior to ionization (v_2) was calculated from the binding energy of Ho M_5 electrons (for $n=3$) and the binding energies of Co, Ni, and Cu L_3 electrons (for $n=2$) [29], since these electrons have the smallest binding energies of their respective shells and, therefore, are the most likely to be ionized. Since the outer-shell electrons are mostly in the N shell, the values of X_n for p_{N+}^x were calculated using the binding energy and the principal quantum number of Ho N_5 electrons. If different binding energies were used, for example, those of L_1, M_1, and N_1 electrons for $n=2$, 3, and 4, respectively, the corrected values of X_n for p_L^x, p_M^x, and p_{N+}^x would decrease by approximately 5, 17, and 12%, respectively. This would move the data points in the horizontal direction somewhat closer to the dashed line in Fig. 5, but as a result, the universality of the scaling would slightly deteriorate.

In the independent electron approximation [26], the cross section (σ_m) for the removal of exactly m electrons from a shell containing N electrons ($m \leqslant N$) is expressed in terms of the single-electron ionization probability $p(b)$ as

$$\sigma_m = 2\pi \int_0^\infty \binom{N}{m} p(b)^m [1-p(b)]^{N-m} b\,db, \tag{4}$$

where b is the impact parameter. If $p(b)$ is approximated by an exponential decay function [33],

$$p(b) = p_o \exp(-b/r), \tag{5}$$

in which p_o and r are parameters that do not depend on b, then

$$\sigma_m = 2\pi r^2 \binom{N}{m} p_o^m \sum_{i=0}^{N-m} (-1)^i \binom{N-m}{i} p_o^i/(m+i)^2. \tag{6}$$

In this approximation, the *ratio* σ_2/σ_1 depends only on p_o and not on r. The parameter $p_o = p(0)$ is the ionization probability per electron at impact parameter equal to zero, and therefore it can be approximated by the parameter p_s^x given by Eq. (3) under the assumptions discussed in Sec. IV.

The solid lines in Fig. 6(a) represent the values of σ_2/σ_1 for L-vacancy production in Ho and K-vacancy production in Ni, calculated using Eq. (6) and plotted as a function of p_o. They are compared to the measured $R^L{}_{2/1}$ and $R^K{}_{2/1}$, for which the corresponding values of p_o (i.e., p_s^x) were determined using Eq. (3). The calculations agree with both sets of measured data reasonably well. Predicted values of σ_2/σ_1 can also be presented as universal functions of X_n by expressing p_o in Eq. (6) in terms of the universal variable, using either the empirical curve [Eq. (3)] or the geometrical model curve [Eq. (1)]. Both results are shown in Fig. 6(b) and compared to the experimental data.

VI. CONCLUSIONS

Spectra of L x rays emitted from Ho targets bombarded by 10 keV electrons and 6 MeV/amu C, Ne, Ar, Kr, and Xe ions were measured in high resolution using a curved crystal spectrometer. Interpretation of the spectra induced by the heavy ion beams was based on the independent electron approximation and the results of Dirac-Fock calculations. This approach resulted in a satisfactory representation of all the major structural features in the spectra. It was found that transitions from atoms with single L- and multiple M+ outer-shell vacancies in the initial state dominate the spectra. In addition, contributions of up to 21% of the total intensity, from L x rays emitted by atoms with two or three L vacancies in the initial state, were clearly identified. Significant contributions (typically ~4% of the total intensity) from diagram lines originating from photoionization and ionization by secondary electrons were found in the spectra induced by Ne, Ar, Kr, and Xe ions. In the spectrum induced by C ions, the satellite peaks arising from $L\beta_1$ and $L\beta_2$ x-ray emission in the presence of a single-spectator M vacancy were seen resolved.

M-shell and outer-shell apparent average vacancy fractions in near-central collisions (p_M^x and p_{N+}^x) were obtained in the analyses of the spectra of Ho L x rays and compared to L-shell apparent average vacancy fractions (p_L^x) obtained in similar analyses of Co, Ni, and Cu K x-ray spectra excited by the same heavy ion beams. It was found that the values of p_L^x, p_M^x, and p_{N+}^x lie on a universal curve when scaled according to the geometrical model. However, the actual predictions of the geometrical model for the corresponding ionization probabilities per electron (p_L, p_M, and p_{N+}) were found to increasingly overestimate the experimental data points as the universal variable increased beyond 0.5 (in atomic units).

Using a model based on the independent electron approximation with the assumption that the relevant ionization probabilities are exponential decay functions of the impact pa-

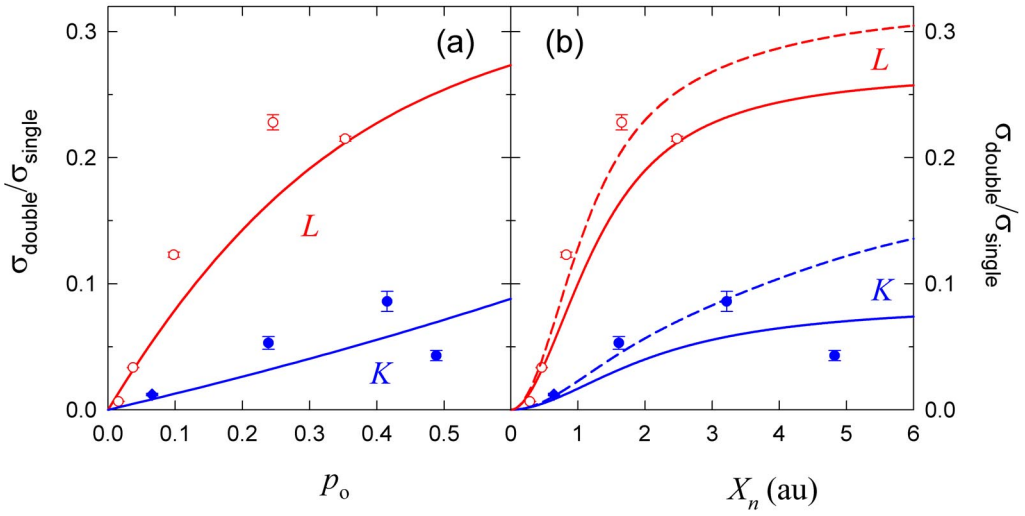

FIG. 6. (Color online) Double-vacancy production to single-vacancy production cross-section ratios (σ_2/σ_1), calculated using Eq. (6), plotted (a) as a function of the single-electron ionization probability at small impact parameters (p_o) and (b) as a function of the corresponding universal variable (X_n) determined using Eq. (3). The solid lines represent the results for the *L*-shell ionization of Ho (red) and *K*-shell ionization of Ni (blue). Also shown are the measured values of $R^L{}_{2/1}$ (open circles) and $R^K{}_{2/1}$ (solid circles), for which X_n was determined using Eq. (2) and the corresponding values of p_o were determined as p_s^x using Eq. (3). The data point shown by the solid diamond (measured using a 6 MeV/amu N beam on a Ni target) was taken from Ref. [34]. The dashed lines represent the universal function predicted by the geometrical model, as given by Eq. (1).

rameter, it was found that the average double-vacancy production to single-vacancy production cross-section ratios can be expressed in terms of the single-electron-ionization probability at small impact parameters or as a function of the geometrical model universal variable. Predictions of the model agree reasonably well with both sets of measured data. General validity of these results remains to be tested experimentally for different collision parameters.

ACKNOWLEDGMENT

This work was supported by the Robert A. Welch Foundation.

APPENDIX: DETAILS OF THE LEAST-SQUARES FITTING METHOD IN THE ANALYSIS OF THE SPECTRA

Individual $L^1\xi M^j$ satellite peaks were represented by Voigt functions having Lorentzian widths equal to those of their corresponding diagram lines. Gaussian widths of the Voigt functions were adjusted to account for the gross effects of outer-shell ionization and multiplet splitting. Specifically, they were parametrized using the following expression:

$$(\sigma_j^\xi)^2 = (\sigma_o^\xi)^2 + j(18-j)[(\sigma_1^\xi)^2 - (\sigma_o^\xi)^2]/17, \quad (j \geqslant 2) \tag{A1}$$

in which σ_0^ξ and σ_1^ξ are the parameters of the fit representing, in principle, the Gaussian widths of the $L^1\xi M^o$ and $L^1\xi M^1$ satellite peaks, respectively. For simplicity, the two parameters were assumed to have common values within each of three groups of transition types classified according to transition energy. The first group included α_2, α_1, and η; the second group included β_4, β_1, β_6, and β_3; and the third group included β_{15} and β_2. The second term in Eq. (A1) approximately accounts for the fact that multiplet splitting causes the Gaussian width of a satellite peak to depend on the number of *M* vacancies. Because the number of allowed transitions in a multiplet is expected to be about the same for configurations containing *j* spectator *M* vacancies or *j* spectator *M* electrons (18-*j* vacancies), this correction was taken to be proportional to $j(18\text{-}j)$.

For a given transition (specified by ξ) the relative number of counts in each $L^1\xi M^j$ satellite peak was assumed to follow a binomial distribution as a function of the number of spectator *M* vacancies (j). It was assumed that this distribution, characterized by its centroid (p_M^x) is the same for all transitions. The parameter p_M^x is interpreted to be the apparent average *M*-vacancy fraction at the time of *L* x-ray emission. The relative intensities of peaks due to transitions to the same *L* subshell were kept fixed at the values given in Ref. [23]. The background in the spectra shown in Figs. 1(d) and 1(e) was parametrized as a linear function of energy, whereas that in the spectra shown in Figs. 1(b) and 1(c) had to be described by an exponential decay function plus a constant.

Determination of the centroids of the $L^i\xi M^j$ satellite peaks was based on a set of reference values, $(E^\xi_{i,j,k})_{\text{calculated}}$, obtained for each transition type ξ using the MCDF program of Desclaux [24]. The calculations were performed in the average-of-configurations mode with configuration interaction. Initial state configurations included those with single ($i=1$) and double ($i=2$) *L* vacancies and either (i) 0, 1, 16, and 17 spectator *M* vacancies (for $L \rightarrow M$ transitions) or (ii) 0, 1, 17, and 18 spectator *M* vacancies (for $L \rightarrow N$ transitions). The spectator vacancies were distributed statistically over the *M* subshells. The vacancy population of the outer shells (k) was the same as in the ground state of the neutral atom (i.e., $k=0$). Reference values of transition energies for

other degrees of M-shell ionization (j) were obtained from the calculated energies for the cases mentioned above by interpolation using a cubic polynomial.

Since the outer shells were assumed to have no missing electrons in the initial states, the calculated reference energies for $i=1$ and $k=0$ represent the lowest possible centroid energies of the $L^1\xi M^j$ satellites. To obtain centroids of the actual $L^1\xi M^j$ satellite peaks, the reference energies need to be corrected for the effects of outer-shell ionization. In view of the uncertainties associated with the calculated transition energies and the lack of information about the distribution of outer-shell vacancies, it was assumed that the centroids of the $L^1\xi M^j$ satellite peaks, $(E^{\xi}_{1,j,\kappa})_{\text{observed}}$, corresponding to the *average* number of outer-shell spectator vacancies (κ), could be approximated reasonably well by adding a correction term to the calculated reference energies, $(E^{\xi}_{1,j,0})_{\text{calculated}}$, so that for any given transition type ξ and a specified number of spectator M vacancies j ($j=0$–18 for $L\rightarrow N$ transitions or 0–17 for $L\rightarrow M$ transitions)

$$(E^{\xi}_{1,j,\kappa})_{\text{observed}} = (E^{\xi}_{1,j,0})_{\text{calculated}} + \kappa\varepsilon^{\xi}_{j}. \tag{A2}$$

The last term in Eq. (A2) is to correct the satellite energy for outer-shell ionization, assuming that κ is the same for all values of j. The energy shift of the $L^1\xi M^j$ satellite peak per outer-shell spectator vacancy [ε^{ξ}_{j} in Eq. (A2)] was estimated using the expression

$$\varepsilon^{\xi}_{j} = [(j_{\max}-j)\varepsilon^{\xi}_{\min} + j\varepsilon^{\xi}_{\max}]/j_{\max}, \tag{A3}$$

where

$$\varepsilon^{\xi}_{\min} = [(E^{\xi}_{1,0,k_{\max}})_{\text{calculated}} - (E^{\xi}_{1,0,0})_{\text{calculated}}]/k_{\max} \tag{A4}$$

and

$$\varepsilon^{\xi}_{\max} = [(E^{\xi}_{1,j_{\max},k_{\max}})_{\text{calculated}} - (E^{\xi}_{1,j_{\max},0})_{\text{calculated}}]/k_{\max}, \tag{A5}$$

are, respectively, the minimum and maximum transition energy shifts per outer-shell vacancy. In the expressions above, $j_{\max}=17, k_{\max}=39$ for $L\rightarrow M$ transitions, while for $L\rightarrow N$ transitions $j_{\max}=18, k_{\max}=38$. The calculated values of $\varepsilon^{\xi}_{\min}$ and $\varepsilon^{\xi}_{\max}$ are listed in Table III. Calculations of $E^{\xi}_{1,0,k\max}$ and $E^{\xi}_{1,j\max,k\max}$ were performed using the method described above for the reference energies.

The average number of outer-shell spectator vacancies (κ) was determined in the fitting procedure in the case of the C- and Ne-induced spectrum [Figs. 1(b) and 1(c)]. In the analyses of the other spectra, this parameter was found to have a strong dependency on p^x_M. Such behavior was not surprising because the satellite distribution in those spectra is devoid of structure and can be well described by a single peak. Therefore, a large increase in the value of κ can be fully compensated by a relatively small decrease in the value of p^x_M without significantly affecting the quality of the fit. In order to obtain reasonable best-fit values of these two parameters in those cases, it was assumed that p^x_M and κ are related to each other according to Eqs. (1) and (2) for M- and N-shell ionization probabilities per electron (p_M and p_N, respectively).

TABLE III. Minimum and maximum energy shift ($\varepsilon_{\min}$ and $\varepsilon_{\max}$, respectively) of the $L^1\xi M^j$ satellites per outer-shell vacancy.

Transition type (ξ)	$\varepsilon_{\min}$(eV)	$\varepsilon_{\max}$(eV)
α_1	2.3	5.1
α_2	2.3	5.0
β_6	9.0	18.1
β_2	9.2	16.6
β_{15}	9.2	16.5
β_1	2.4	5.3
η	2.9	6.9
β_3	2.7	6.2
β_4	2.5	5.7

The values of p_M and p_N were calculated for the ionization of $M_5(n=3)$ and $N_5(n=4)$ electrons of Ho, respectively, by projectiles ranging in atomic number from 1 to 92 using Eq. (1). The calculated p_N values were then plotted versus the calculated p_M values, and the resulting data points were fit by a second-order polynomial passing through the origin. It was found that p_N can be estimated from the corresponding value of p_M using the expression

$$p_N = 1.16p_M - 0.150p^2_M. \tag{A6}$$

The data points were below the curve defined with Eq. (A6) by 4 to 1% for p_M between 0 and 0.2 and deviated by less than ±1% for other values of p_M. Then it was assumed that Eq. (A6) holds when p_N is replaced by p^x_{N+}, while p_M is replaced by p^x_M, so that

$$\kappa = k_{\max} \times [1.16p^x_M - 0.150(p^x_M)^2]. \tag{A7}$$

Contributions to the spectra from multiple L ionization were found to be small in all cases studied here. Therefore, they were described with much less sophistication. It was assumed that the $L^i\xi M^j$ satellites having $i>1$ could be described in the same way as those corresponding to $i=1$, only scaled down in intensity. The same scaling factor was applied to all peaks, and its best value was determined from the fit. Energy shifts of the $L^2\xi M^j$ satellites were estimated using the same procedure as described earlier for the $L^1\xi M^j$ satellites. The $L^3\xi M^j$ satellites were considered only if their inclusion led to significant improvement of the fit (which was the case for the spectra of Ho L x rays induced by Ar, Kr, and Xe projectiles). Energy shifts per spectator L vacancy for the $L^3\xi M^j$ satellites were assumed to be the same as those for the $L^2\xi M^j$ satellites. Satellites for $i\geqslant 4$ were not considered in this work.

[1] See F. K. Richtmyer, Rev. Mod. Phys. **9**, 391 (1937).
[2] L. G. Parratt, Phys. Rev. **50**, 598 (1936).
[3] L. G. Parratt, Phys. Rev. **54**, 99 (1938).
[4] C. A. Randall and L. G. Parratt, Phys. Rev. **57**, 786 (1940).
[5] D. Coster and R. de L. Kronig, Physica (Utrecht) **2**, 13 (1935).
[6] F. K. Richtmyer and E. G. Ramberg, Phys. Rev. **51**, 925 (1937).
[7] E. L. Feinberg, J. Phys. (USSR) **4**, 423 (1941); A. Migdal J. Phys. (USSR) **4**, 449 (1941).
[8] M. H. Chen, B. Crasemann, M. Aoyagi, and H. Mark, Phys. Rev. A **15**, 2312 (1977).
[9] J. Tulkki and O. Keski-Rahkonen, Phys. Rev. A **24**, 849 (1981).
[10] P. Putila-Mantyla and G. Graeffe, Phys. Rev. A **39**, 1149 (1989).
[11] H. Oohashi, T. Tochio, Y. Ito, and A. M. Vlaicu, Phys. Rev. A **68**, 032506 (2003).
[12] R. C. Der, R. J. Fortner, T. M. Kavanah, and J. M. Khan, Phys. Lett. **36A**, 239 (1971).
[13] D. K. Olsen, C. F. Moore, and P. Richard, Phys. Rev. A **7**, 1244 (1973).
[14] T. M. Rosseel, J. M. Dale, H. W. Dunn, L. D. Hulett, Jr., S. Kahane, H. F. Krause, S. Raman, G. G. Slaughter, C. R. Vane, and Y. P. Young, Nucl. Instrum. Methods Phys. Res. B **3**, 94 (1984).
[15] T. M. Rosseel, J. M. Dale, L. D. Hulett, H. F. Krause, P. L. Pepmiller, S. Raman, C. R. Vane, and J. P. Young, Nucl. Instrum. Methods Phys. Res. B **10/11**, 195 (1985).
[16] Ch. Heitz, J. Larcher, G. J. Costa, A. Pape, Y. El Masri, Th. Keutgen, I. Tilquin, F. Hanappe, and P. Duhamel, Z. Phys. D: At., Mol. Clusters **42**, 15 (1997).
[17] M. Czarnota, M. Pajek, D. Banas, D. Chmielewska, J. Rzadkiewicz, Z. Sujkowski, J.-Cl. Dousse, M. Berset, O. Mauron, Y.-P. Maillard, P. A. Raboud, J. Hoszowska, M. Polasik, and K. Slabkowska, Nucl. Instrum. Methods Phys. Res. B **205**, 133 (2003).
[18] D. Banas, J. Braziewicz, M. Pajek, J. Semaniak, T. Czyzewski, I. Fijal, M. Jaskola, W. Kretschmer, T. Mukoyama, and D. Trautmann, J. Phys. B **35**, 3421 (2002); B. Banas, M. Pajek, J. Semaniak, J. Braziewicz, A. Kubala-Kukus, U. Majewska, T. Czyzewski, M. Jaskola, W. Kretschmer, T. Mukoyama, and D. Trautmann, Nucl. Instrum. Methods Phys. Res. B **195**, 233 (2002); D. Banas, J. Braziewicz, U. Majewska, M. Pajek, J. Semaniak, T. Czyzewski, M. Jaskola, W. Kretschmer, T. Mukoyama, and D. Trautmann, J. Phys. B **33**, L793 (2000); B. Banas, J. Braziewicz, U. Majewska, M. Pajek, J. Semaniak, T. Czyzewski, M. Jaskola, W. Kretschmer, and T. Mukoyama, Nucl. Instrum. Methods Phys. Res. B **154**, 247 (1999); J. Semaniak, J. Braziewicz, M. Pajek, T. Czyzewski, L. Glowacka, M. Jaskola, M. Haller, R. Karschnick, W. Kretschmer, Z. Halabuka, and D. Trautmann, Phys. Rev. A **52**, 1125 (1995).
[19] R. L. Watson, J. M. Blackadar, and V. Horvat, Phys. Rev. A **60**, 2959 (1999).
[20] V. Horvat and R. L. Watson, J. Phys. B **34**, 777 (2001).
[21] R. D. Deslattes, E. G. Kessler, P. Indelicato, L. de Billy, E. Lindroth, and J. Anton, Rev. Mod. Phys. **75**, 35 (2003).
[22] J. L. Campbell and T. Papp, At. Data Nucl. Data Tables **77**, 1 (2001).
[23] S. I. Salem, S. L. Panossian, and R. A. Krause, At. Data Nucl. Data Tables **14**, 91 (1974).
[24] J. P. Desclaux, Comput. Phys. Commun. **9**, 31 (1975).
[25] V. Horvat, R. L. Watson, and J. M. Blackadar, Nucl. Instrum. Methods Phys. Res. B **170**, 336 (2000); M. Kobal, M. Kavcic, M. Budnar, J.-Cl. Dousse, Y.-P. Maillard, O. Mauron, P.-A. Raboud, and K. Tokesi, Phys. Rev. A **70**, 062720 (2004); R. L. Watson, V. Horvat, J. M. Blackadar, and K. E. Zaharakis, *ibid.* **62**, 052709 (2000).
[26] J. H. McGuire and L. Weaver, Phys. Rev. A **16**, 41 (1977).
[27] B. Sulik, I. Kadar, S. Ricz, D. Varga, J. Vegh, G. Hock, and D. Berenyi, Nucl. Instrum. Methods Phys. Res. B **28**, 509 (1987).
[28] J. H. McGuire and P. Richard, Phys. Rev. A **8**, 1374 (1973).
[29] J. A. Bearden and A. F. Burr, Rev. Mod. Phys. **39**, 125 (1967).
[30] F. Ziegler (1996), *program SRIM*, http://www.srim.org/
[31] W. Brandt and G. Lapicki, Phys. Rev. A **23**, 1717 (1981); G. Lapicki and F. D. McDaniel, Phys. Rev. A **22**, 1896 (1980).
[32] M. J. Berger and J. H. Hubbell, *program XCOM*, http://physics.nist.gov/XCOM
[33] T. Tonuma, H. Shibata, S. H. Be, H. Kumagai, M. Kase, T. Kambara, I. Kohno, A. Ohsaki, and H. Tawara, Phys. Rev. A **33**, 3047 (1986).
[34] Y. Awaya, T. Kambara, Y. Kanai, Int. J. Mass. Spectrom. **192**, 49 (1999).